PNAS RESEARCH ARTICLE | CHEMISTRY

Thioether editing generally increases the photostability of rhodamine dyes on self-labeling tags

Jing Ling[a,1], Yuan Zhang[b,1,2], Yongzhen Hei[c,1], Julian Kompa[d], Chen Yang[c], Bo Wang[a,e,f], Junwei Zhang[b], Jiasheng Du[b], Tatjana Rudi[g], Kecheng Zhang[a,b], Jingfu Sun[h,i], Wenjuan Wang[j], Sebastian Fabritz[g], Yulong Li[a,k,l,m], Wulan Deng[a,e,f], Peng Zou[a,l,m,n], Chunlai Chen[c,2], and Zhixing Chen[a,b,h,i,k,o,2]

Affiliations are included on p. 11.

Edited by Philip Tinnefeld, Ludwig-Maximilians-Universität München, München, Germany; received December 22, 2024; accepted June 2, 2025 by Editorial Board Member Yale E. Goldman

Self-labeling protein tags are widely used in advanced bioimaging where dyes with high-photon budgets outperform their fluorescent protein counterparts. Further increasing the emitted photon numbers of dye-tag systems is actively pursued by both new fluorophore chemistry and protein engineering. By scrutinizing the protein microenvironment of fluorophores, here we propose that proximal thioether groups negatively affect the photostability of the dye-tag system. We attribute the disparity in photostability of rhodamine dyes on HaloTag, SNAP-tag, and TMP-tag3 to the influence of the inherent thioether linkage within the SNAP-tag and TMP-tag3. This photochemical pathway leads us to further devise tags with higher photostability. We first show that rhodamine dyes on TMP-tag3.1, which employs a proximity-induced SuFEx reaction instead of a thiol-acrylamide addition to replace the thioether adduct, achieve photon budgets comparable to those ligands on HaloTag. We further showcase that by mutating the methionine near the fluorophore pocket, HaloTag: M175L generally gives up to four times enhancement on photostability when labeled with red and far-red rhodamines. The enhancement of HaloTag modification is demonstrated with single-molecule fluorescence imaging, live-cell fluorescence imaging, and voltage imaging. During time-lapse imaging, gradual photooxidation of Met leads to a reduced photobleaching rate, mechanistically supporting the thioether pathway hypothesis. Our findings suggest that thioether editing on self-labeling tags is a general strategy to enhance the photostability of fluorophores for advanced time-lapse imaging techniques.

self-labeling protein tags | photostability | thioether editing | protein microenvironment | rhodamine dyes

Significance

Self-labeling protein tags (SLPs) are popular tools in fluorescence imaging, particularly in applications requiring high photon budgets. Previously, efforts to improve the photostability of dye-tag systems have primarily focused on the molecular engineering of fluorophores. Here, we identify the thioethers as one of the determinants of photostability in SLPs. By employing a thioether-editing strategy on TMP-tag3 and HaloTag, rhodamine dyes on SLPs can generally reach enhanced photon budgets. Notably, eliminating a thioether by mutating Met 175 on HaloTag to Leu gave an up to fourfold increase in photostability, as demonstrated by applications in single-molecule imaging, live-cell fluorescence imaging, and voltage imaging.

Modern fluorescence imaging enables the real-time visualization of the localization, dynamics, and functions of biological macromolecules in living cells. This accomplishment necessitates the parallel development and advancement of microscopy techniques and fluorescent molecules. Beyond genetically encodable fluorescent proteins, one of the most commonly used labeling methods for recording biomolecules in living cells are self-labeling protein (SLP) tags (1–4). The widely used SLP systems are HaloTag (5), SNAP-tag (6), and TMP-tag (7, 8), offering several advantages over fluorescent proteins including higher brightness, greater photostability, and a broader spectrum of fluorophores. Consequently, SLPs are particularly suitable for super-resolution live-cell imaging, where the photostability of synthetic dyes made them privileged choices under strong excitation lights (4, 9).

In modern imaging techniques that demand a high photon budget, photobleaching of fluorescent molecules reemerges as a major challenge. The most studied pathways for fluorophore photobleaching involve their triplet states and the sensitized singlet oxygen (10–12). For example, Cy5 and Cy7 bleach through 2 + 2 cycloaddition reactions with singlet oxygen, which subsequently yield in C–C cleavage (13). Meanwhile, for rhodamine dyes, the stepwise photochemical oxidation and N-dealkylation are well-explored photobleaching pathways (14). As both the pathways occur in the presence of oxygen, adding oxygen scavengers and triplet state quenchers (TSQs) to the solution can alleviate photobleaching and enhance photon budgets for selected dyes (15, 16). Further along this line, TSQ-dye covalent conjugates are emerging molecules for live-cell imaging, thanks to their lower phototoxicity, yet their photostabilities are shown to be highly dependent on the dye structures (17, 18). Based on these mechanistic insights into photobleaching, chemists have made substantial progress through the modification of the structure of fluorophores to improve photostability (14, 19–27).

Competing interest statement: C.C., Z.C., Y.Z., and C.Y. are the inventors of a patent on the fluorophores with S-arylation-type conjugation chemistry (CN202210228995.1, patent pending), whose value may be affected by this paper.

This article is a PNAS Direct Submission. P.T. is a guest editor invited by the Editorial Board.

[1]J.L., Y.Z., and Y.H. contributed equally to this work.

[2]To whom correspondence may be addressed. Email: zhangyuan19@pku.edu.cn, chunlai@mail.tsinghua.edu.cn, or zhixingchen@pku.edu.cn.

This article contains supporting information online at https://www.pnas.org/lookup/suppl/doi:10.1073/pnas.2426354122/-/DCSupplemental.

Published July 18, 2025.

In parallel to the core structure of dyes, recent works have suggested that the protein microenvironment surrounding a fluorophore can significantly influence its photophysical properties. Various factors, including the bioconjugation linkage between the protein and the dye and the neighboring amino acid residues, can affect brightness (28), fluorescence lifetime (29), and chemical equilibrium of dyes (30, 31). Furthermore, the photostability of fluorophores can also be influenced by the microenvironment of surrounding biomacromolecules. Recent advancements such as ultraphotostable fluorescent protein StayGold (32) and DNA FluoroCube (33, 34) have demonstrated remarkably high photostability due to the optimization of their microenvironments. In our previous research, we demonstrated that the presence of a thioether group in the maleimide-thiol bioconjugation linker significantly diminishes the photostability of the dyes. In addition, we reported that the total emitted photons of the same dye labeled on different proteins or different positions on the same proteins can vary up to five folds (35). These data collectively suggest that the protein microenvironment plays an important role in the photostability of the dye. We therefore speculate that the SLP systems can be potentially engineered toward higher photostability by tuning the protein microenvironments of the labeled dye. In particular, as SNAP-tag features a thioether linker while HaloTag exploits an ester bond, the thioether photobleaching pathway we unveiled may contribute to the well-documented difference in photostability between these two SLPs (36, 37).

Here, we examined the impact of nearby thioether groups on dye photostability in SLPs. We confirmed the disparities in their photostability under single-molecule conditions for the Halo, SNAP, and TMP3-rhodamine complexes. Furthermore, tuning the electronic properties of the thioether linkage can enhance the photostability of fluorescent dyes in the TMP-tag system. Subsequently, we substituted the thiol-acrylamide-based conjugation chemistry with a SuFEx reaction, which eliminates the thioether in the linker. The photon budgets of our engineered TMP-tag3.1 were higher than those of TMP-tag3 and comparable to those of dye-HaloTag conjugates. On HaloTag, we showed that the introduction of Met residues near the dye significantly diminishes photostability, recapitulating the thioether effect. Guided by the thioether effect, replacing an M175 residue near the dye pocket in HaloTag7 with selected amino acids generally improved the photostability of labeled rhodamine dyes. We specifically highlighted HaloTag M175L with a palette of rhodamine fluorophores, whose outstanding photostability enables general use in time-lapse imaging including highly sought-after applications such as voltage imaging and superresolution imaging such as Hessian-SIM live-cell imaging. Finally, we characterized the photooxidation of surface Met residues on HaloTag in the presence of a SiR-dye and proposed a methionine-based mechanism for the difference in photobleaching rates between the early and late stages of time-lapse fluorescent imaging.

Results

Rhodamine Dyes Exhibit Notable Variations in Photostability on Different Self-Labeling Tags. The optical properties of dyes can be significantly influenced by their microenvironment, which is related to both the nearby residues and the labeling strategies. The covalent labeling of HaloTag involves the nucleophilic attack of the carboxyl group in the Asp106 to an alkyl chloride in the ligand, resulting in the formation of an ester adduct (Fig. 1*A*) (5). For SNAP-tag, the O^6-alkyl group is transferred from the alkylguanine substrate to the cysteine residue via an S_N2 mechanism (Fig. 1*A*). The noncovalent TMP-tag was developed through the integration of noncovalent interactions with the small molecule trimethoprim and its target protein, *Escherichia coli* dihydrofolate reductase (eDHFR) (7). Taking advantage of proximity-induced reactivity, a Cys residue was introduced on the surface of eDHFR (eDHFR: L28C) to form a covalent bond with the neighboring acrylamide electrophile on the TMP conjugates, leading to the generation of a series of covalent TMP-tag (8, 38, 39) (Fig. 1*A*). In our previous work, we demonstrated that the presence of nearby thioethers significantly decreased the photostability of dyes (35) (Fig. 1*B*). Indeed, both SNAP-tag and TMP-tag3 yield a proximal thioether moiety adjacent to the dye as a reaction product, whereas the covalent labeling reaction of HaloTag does not result in the formation of a thioether linkage. Previous studies have reported higher photostability of the same rhodamine dye in the HaloTag system compared to the one in the SNAP-tag (36, 37). We speculate that the presence of inherent thioethers may contribute to the observed differences in photostability between the rhodamine-tag systems.

To investigate the impact of thioethers on the photostability of rhodamine-tag systems and to guide tag engineering with improved photostability, we initially examined two representative rhodamine dyes, tetramethyl rhodamine (TMR) and silicon rhodamine (SiR, Fig. 1*A*), using three different self-labeling tags under two conditions. PBS buffer was employed as a simple and well-defined buffer containing dissolved oxygen, whereas antifade buffer, containing oxygen scavengers and triplet state quenchers, was used to examine the photostability of SLPs with depleted oxygen and triplet-states. Comparison between them would provide further mechanistic insights into photobleaching pathways. Specifically, the HaloTag used in this study is derived from the HT7 variant and the TMP-tag3 is from the previous work in our group (5, 8).

By employing a single-molecule fluorescence assay, we aimed to compare the total emitted photon count per protein-labeled dye molecule under different conditions. This is limited by photobleaching as evidenced by the bleaching time of fluorescence traces (*SI Appendix*, Figs. S1–S4). The HaloTag-labeled rhodamines exhibited higher photostability and higher brightness compared to the other two tags, regardless of the presence of antifade additives (Fig. 1 *C* and *D*). With TMR, HaloTag exhibited a 3.0-fold and 2.3-fold advantage in photostability in the antifade buffer over the SNAP-tag and TMP-tag3 systems, respectively. In PBS, the photostability advantage changed to 3.1-fold and 2.5-fold, respectively. For SiR, HaloTag showed a similar photostability advantage of 2.3-fold (over SNAP-Tag) and 1.7-fold (over TMP-tag3) under antifade conditions and 1.6-fold (over SNAP-Tag) and 3.1-fold (over TMP-tag3) in PBS, respectively (Fig. 1*C*).

The result that SNAP-tag and TMP-tag3 conjugates showed decreased photostability compared to HaloTag conjugates is consistent with our speculation based on our previous findings on thioether-induced photobleaching (35), which pinpointed the formation of inherent thioethers on the linkage of the binding module and the fluorophores as a possible factor to reduce photostability of a series of dyes on tags (Fig. 1*B*).

Thioether Editing Increases the Photostability of the Rhodamine-TMP System. To confirm the impact of alkyl thioethers on the decreased photostability of dye-tag systems, we tested three different labeling strategies Mal (Maleimide), POD (phenyloxadiazole), and TMP-tag3 to label representative rhodamine dyes, TMR and SiR, on the eDHFR (L28C) proteins (Fig. 2*A*). The specificity of labeling can be achieved as the introduced L28C mutation is the only reactive Cys on the surface of eDHFR. Subsequently, the

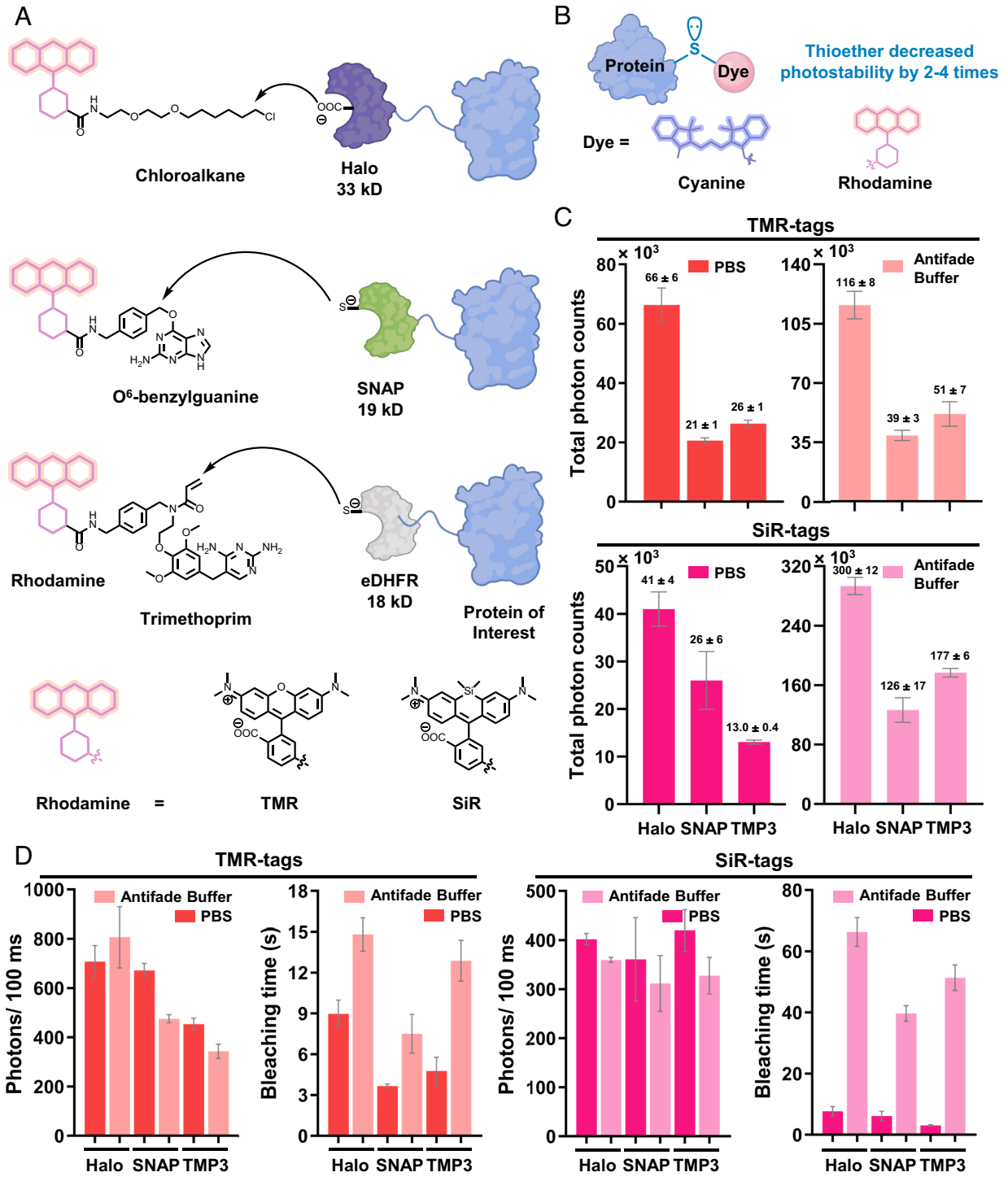

Fig. 1. Photostability of rhodamine dyes varies significantly on different self-labeling tags measured by photon budget at the single-molecular level. (*A*) Labeling biochemistry of HaloTag, SNAP-tag, and TMP-tag3 featuring different nucleophiles. (*B*) Thioether-induced photobleaching pathway affects both rhodamine and cyanine fluorophores as demonstrated in previous studies (35). (*C*) Total emitted photons of TMR and SiR labeled on HaloTag, SNAP-tag, and TMP-tag3 without (PBS) or with the oxygen-scavenging system and triplet-state quenchers (Antifade Buffer: 3 mg/mL glucose, 10 units/mL glucose oxidase, 1,200 units /mL catalase, 1 mM COT, 1 mM NBA, and 1.5 mM Trolox). Error bars represent the SD of three independent experiments. Laser power and time resolution: 10 mW (50 W·cm^{-2} for TMR and 40 W·cm^{-2} for SiR) and 100 ms. (*D*) Intensity (photons/100 ms) and bleaching time of TMR and SiR labeled on HaloTag, SNAP-tag, and TMP-tag3 in PBS or the antifade buffer. Error bars represent the SD of three independent experiments.

labeled eDHFR proteins were examined for their single-molecule photon budget.

The POD strategy generates thio-adduct containing electron-deficient aryl thioethers, which are relatively less influenced by the electron-rich alkyl thioethers present in the Mal and TMP-tag3 labeling strategies (35). When introducing rhodamines to eDHFR via POD chemistry, the brightness of dyes remained unaffected but the photostability of POD-labeled rhodamine dyes was the best among their TMP3 and Mal-labeled counterparts (Fig. 2*B* and *SI Appendix*, Fig. S5). For TMR dyes the photostability improvement achieved with the POD strategy was most pronounced in the antifade buffer showing 6.5-fold and 3.6-fold higher photostability than the Mal and TMP-tag3 strategies, respectively. We note that in PBS, the photostability improvement

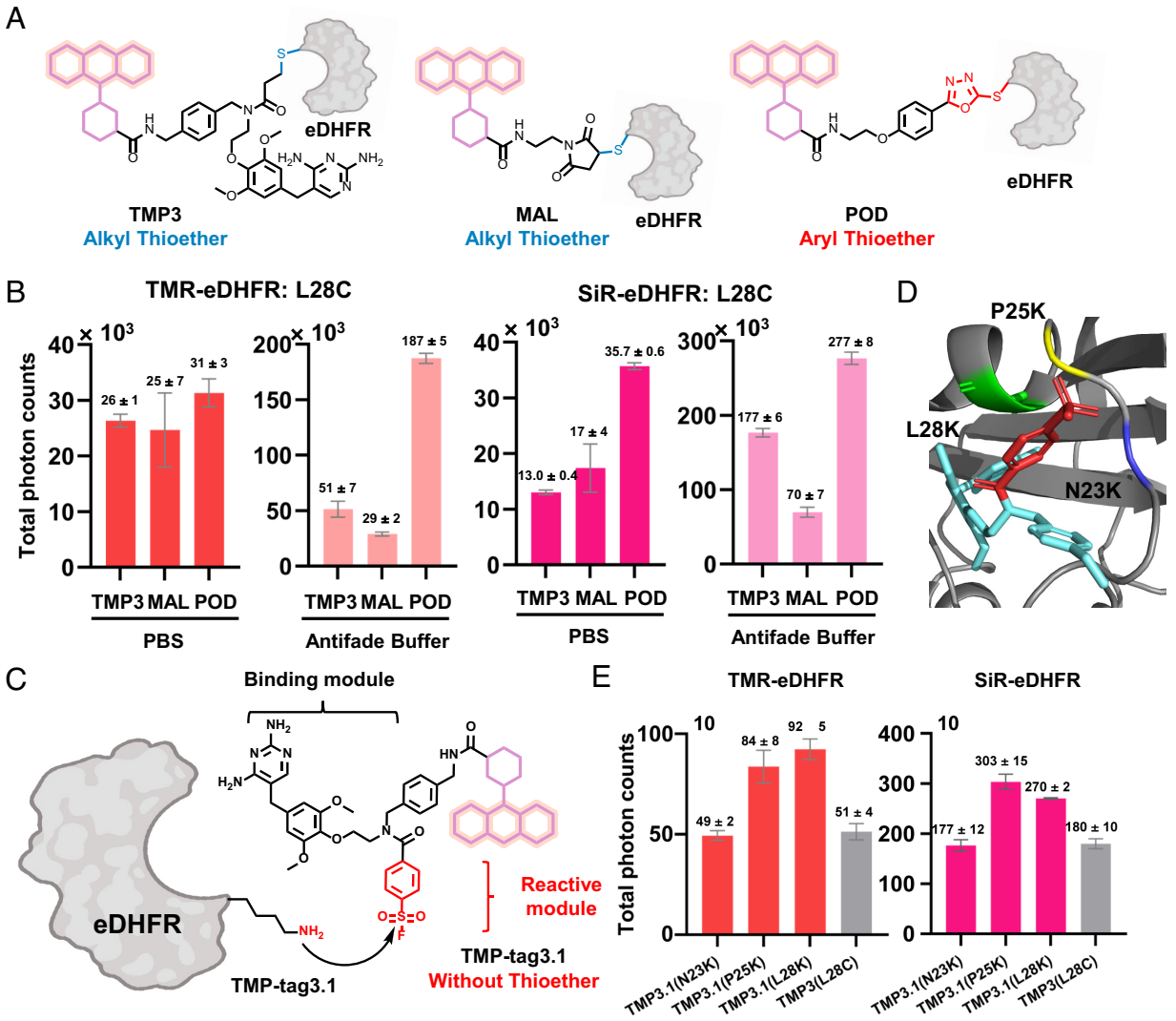

Fig. 2. Thioether-editing strategy enhances the photon budgets of rhodamine dyes labeled on eDHFR. (*A*) Schematic diagram of bioconjugation products resulting from three different labeling strategies: TMP-tag3, MAL, and POD. (*B*) Total emitted photons of TMR and SiR when labeled on eDHFR using TMP-tag3, MAL, and POD labeling strategies in PBS or the antifade buffer. Laser power and time resolution: 10 mW (50 W·cm^{-2} for TMR and 40 W·cm^{-2} for SiR) and 100 ms. (*C*) The proximity-induced labeling reaction of TMP-tag3.1. (*D*) A structural model showing that three adjacent sites may give fast proximal-induced reactivity with TMP-tag3.1. (*E*) Total emitted photons emitted by TMR and SiR, labeled on eDHFR at sites N23K, P25K, L28K, and L28C, are measured with an oxygen-scavenging system and triplet-state quenchers. TMP3: L28C with a thioether adduct serves as a reference. Laser power and time resolution: 10 mW (50 W·cm^{-2} for TMR and 40 W·cm^{-2} for SiR) and 100 ms.

was only 1.3-fold and 1.2-fold, respectively. Regarding SiR dyes, the photostability enhancement with the POD strategy was 2.1-fold and 2.7-fold in PBS and 4.0-fold and 1.6-fold in the antifade buffer relative to the Mal and TMP-tag3 strategies, respectively. (Fig. 2*B* and *SI Appendix*, Figs. S6–S9). Overall, the POD conjugation generally gives better photostability, yet the net gain is dependent on the dye scaffold and protein microenvironments. These data support our hypothesis that thioether is one of the main factors contributing to the faster photobleaching of rhodamines on covalent TMP-tag compared to that of HaloTag.

Encouraged by these results, we proposed that bypassing the Cys-based conjugation chemistry should further reduce the thioether bleaching effect in rhodamine-tag systems. TMP-tag3 contains an independent labeling module, acrylamide, for the formation of alkyl thioethers through the Michael addition reaction. In recent years, significant advancements have been achieved in proximity-induced labeling techniques based on Lys rather than Cys (40–42). Aryl sulfonyl fluoride moieties are designed to undergo sulfur-fluorine exchange reactions with neighboring weakly nucleophilic residues, such as Lys and His (43). Hence, considering the labeling speed and synthetic convenience, we substituted the covalent labeling module in TMP3 with a benzenesulfonyl fluoride module, resulting in the TMP-tag3.1 substrate, that enables covalent labeling with adjacent Lys residues without thioether formation (Fig. 2*C*).

Based on this ligand and eDHFR: L28C, a model was built using Maestro (version 12.0, Schrödinger). Considering the slightly larger size of the benzenesulfonyl fluoride compared to acrylamide, we selected residues L28, along with its neighboring residues at positions P25 and N23, for the introduction of Lys mutations (Fig. 2*D*). Protein mass spectrometry analysis revealed that both the N23K and P25K mutants exhibited faster labeling compared to the L28K protein, achieving half-labeling times under 10 min, which is similar to those of TMP-tag3 (*SI Appendix*, Figs. S10–S13 and Table S1). Moreover, we applied single-molecule assays to quantitatively compare TMP-tag3.1 labeled with TMR and SiR dyes to TMP-tag3. Though the protein environment of the rhodamines may be altered by the different covalent labeling methods, the P25K and L28K-TMP-tag3.1 conjugates yield higher total emitted photons

compared to the TMP-tag3 conjugate by 1.6-fold and 1.8-fold for TMR as well as 1.7-fold and 1.5-fold for SiR. This brings the total emitted photon count of TMP-tag3.1 close to HaloTag labeling with the same dye (Fig. 2*E* and *SI Appendix*, Figs. S14–S17). These results mechanistically support that eliminating thioether can enhance the photostability of SLPs.

Engineering of Proximal Thioether Influences the Photostability of Rhodamine Dyes on HaloTag. To further investigate the impact of thioether groups on rhodamine dyes, we introduced methionine residues onto HaloTag close to the dye binding area and assessed the changes in photostability. Based on the crystal structure of TMR-HaloTag7 (PDB: 6Y7A) (44), we engineered several single-site mutations close to the dye-binding region and conducted single-molecule fluorescence recordings after labeling the mutated proteins with CA-TMR and CA-SiR dyes, respectively. To better present the differences among various mutants, selected single-molecule fluorescence experiments were conducted at a lower power of 1 mW (Fig. 3 *B* and *C*). Under the same dye and buffer conditions, the results obtained at 10 mW power exhibited lower photon budgets and smaller intergroup differences (*SI Appendix*, Fig. S18*C*). The results indicated that mutating proximal residue V167, G171, or T172 to methionine (Fig. 3*A*) gives the most significant reduction in photostability of

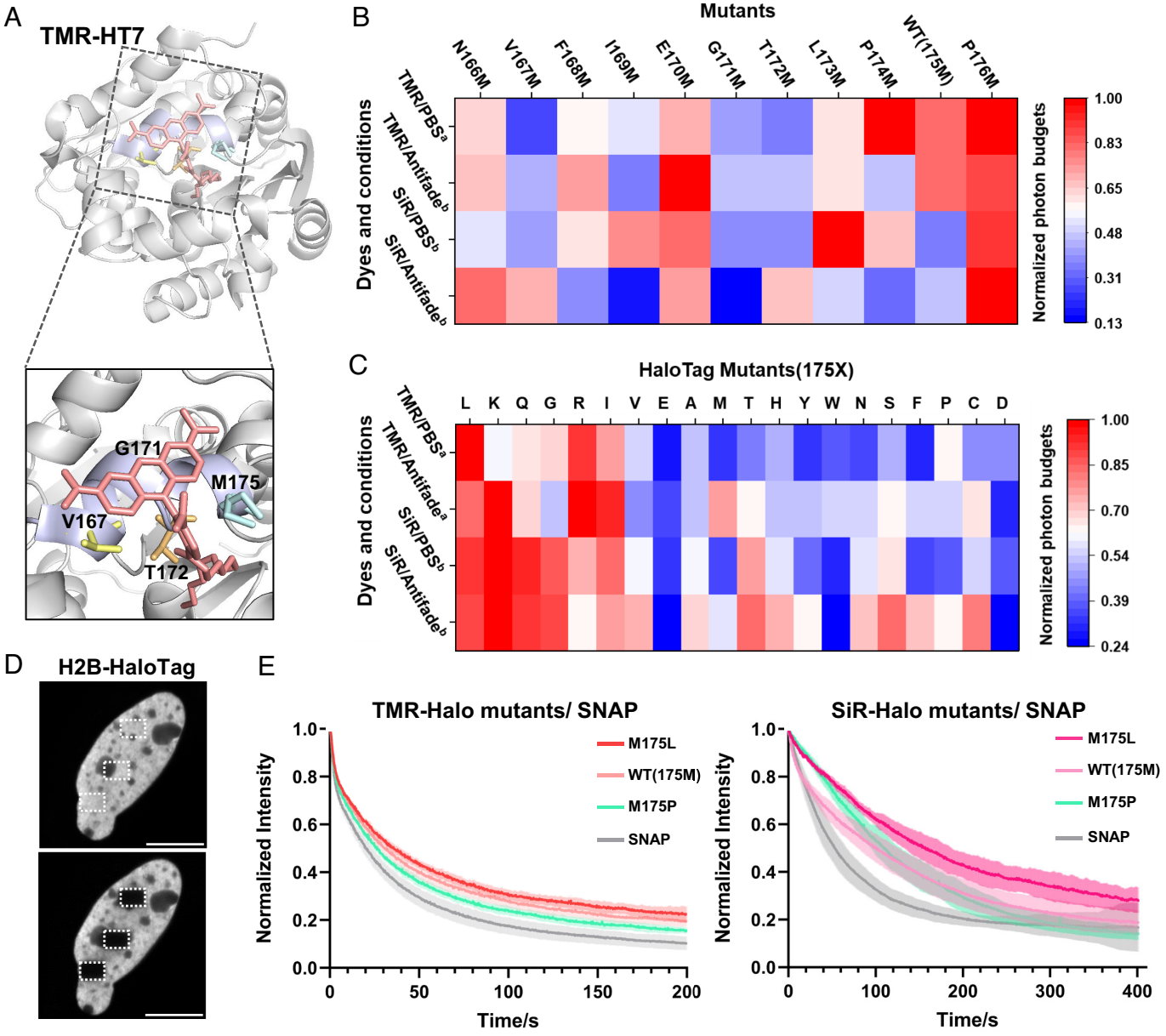

Fig. 3. Proximal thioether editing drastically influences the photostability of rhodamine dyes labeled on Halo mutants. (*A*) Schematic representation of the crystal structure of TMR-HT7 (PDB: 6Y7A). The protein is displayed as a light gray cartoon with relevant residues represented as sticks, the fluorophore ligand is in magenta. The M175 is represented as a cyan stick. (*B*) Normalized photon budgets of TMR and SiR labeled on various X→M mutants of HaloTag in PBS or the antifade buffer. Laser power and time resolution: a) 1 mW (5 W·cm^{-2}) and 1,000 ms; b) 10 mW (50 W·cm^{-2} for TMR and 40 W·cm^{-2} for SiR) and 100 ms. (*C*) Normalized photon budgets of TMR and SiR, labeled on different mutants at site 175 of the HaloTag, are measured in PBS or the antifade buffer. Laser power and time resolution: a) 1 mW (5 W·cm^{-2} for TMR and 4 W·cm^{-2} for SiR) and 500 ms; b) 10 mW (50 W·cm^{-2} for TMR and 40 W·cm^{-2} for SiR) and 100 ms. (*D*) Fluorescence images of HaloTag-expressing nuclei labeled with CA-dyes before (*Top*) and after (bottom) continuous live confocal imaging. Dashed boxes delineate the area subjected to photobleaching by confocal lasers. (Scale bar, 10 μm.) (*E*) Normalized fluorescent decay curves of H2B-Halo-M175X with CA-TMR (*Left*) and CA-SiR (*Right*). Error bars represent SEM (n = 6).

rhodamine-HaloTag in PBS (Fig. 3*B*). In the antifade buffer, for CA-TMR, single-site mutations to Met at residues V167, I169, G171, T172, L173, and P174 resulted in similar decreases in photostability (Fig. 3*B* and *SI Appendix*, Fig. S18). On the other hand, for CA-SiR, the mutation to Met at residue T172 exhibited the poorest photostability (Fig. 3*B* and *SI Appendix*, Fig. S19). Therefore, our experiments demonstrated that the introduction of methionine close to the dye-binding region significantly reduced the photostability of TMR and SiR on HaloTag, and this effect is more pronounced in the presence of the antifade buffer. Notably, the tested mutated sites were at the alpha helix closest to the dye-binding region. The overall trend in the total emitted photons of TMR and SiR on HaloTag mutants exhibited a periodical variation of every 3 or 4 amino acids, which matches the 3.6-residue-per-turn characteristic of α-helices. This finding further supports that the thioether photobleaching pathway is sensitive to spatial factors.

Moreover, we tested whether it was possible to enhance the photostability by eliminating the parental methionine residue (M175) that was spatially adjacent to the rhodamine binding site (Fig. 3*A*). M175 were subjected to saturation mutagenesis, giving a library of 19 HaloTag variants which were purified, labeled with TMR/SiR, and tested in single-molecule imaging. Consistent with our speculation, although M175 is not the closest residue to the dye, eliminating M175 through site-directed mutagenesis can improve total photon counts in most of the cases (Fig. 3*C* and *SI Appendix*, Figs. S20 and S21). Additionally, besides methionine (M), certain other amino acids also exhibit similar negative effects.

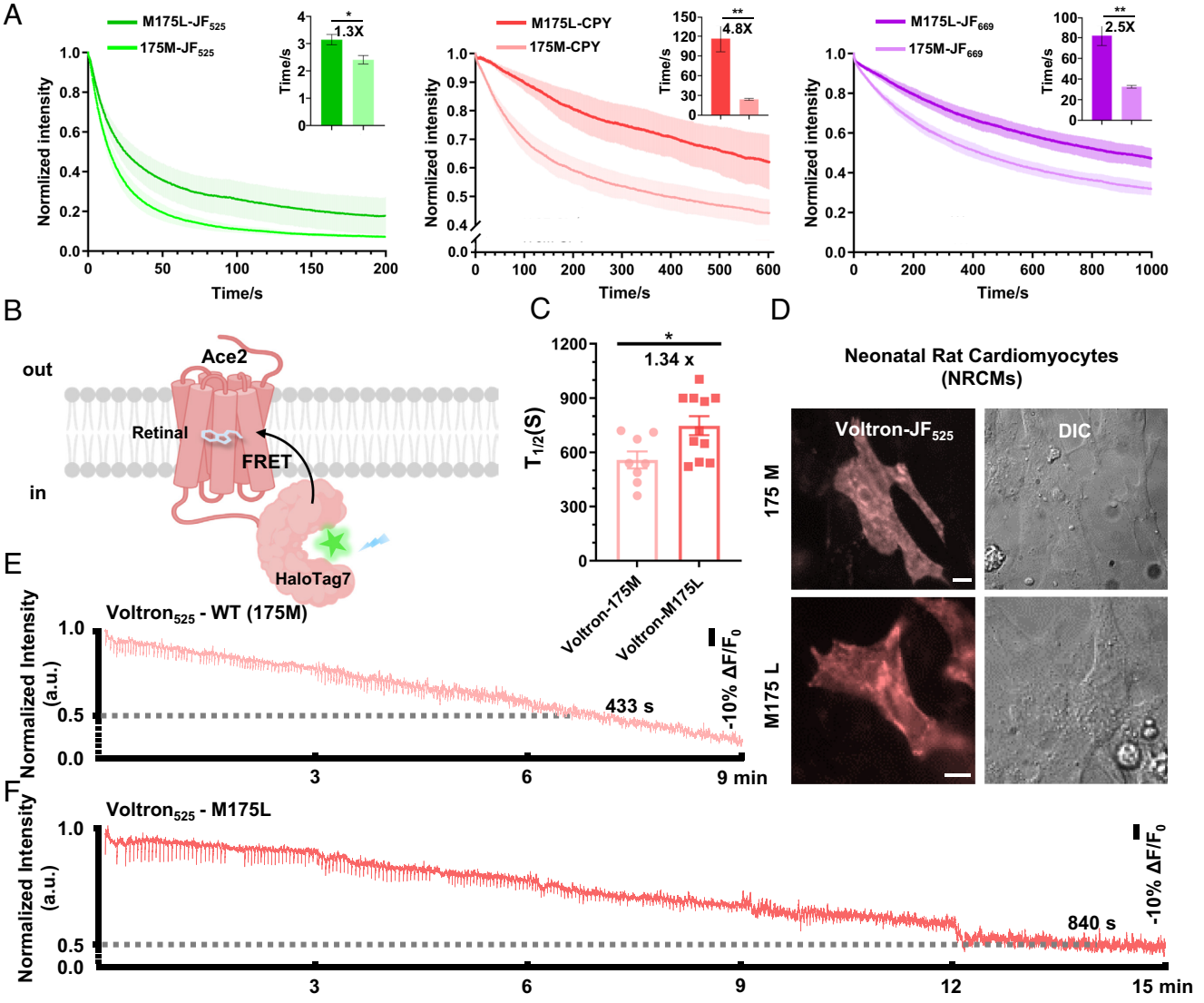

Fig. 4. HaloTag: M175L generally strengthens the photostability of the rhodamine palette. (*A*) Normalized fluorescent decay curves of H2B-Halo-M175X labeled with JF_{525}/CPY/JF_{669} during time-lapse imaging in live cells under confocal microscopy. The error bars represent the SD from six independent experiments. The embedded histogram showed the time required for photobleaching to 90% maximal fluorescence intensity. Statistical significances were calculated with the two-tailed Mann–Whitney U test, and a *P*-value of <0.05* was considered significant. (*B*) Schematic illustration of Voltron, a chemigenetic voltage indicator. (*C*) The time required to bleach 50% of maximum fluorescence ($t_{1/2}$) of NRCMs expressing Voltron (Ace2-HaloTag7)-175 M/M175L labeled with JF_{525}. The illumination intensity of the 488 nm laser was 1.8 $W{\cdot}cm^{-2}$, and the camera frame rate was 100 Hz. The bars indicate the mean of eight or eleven cells, and the error bars represent the SEM. The significance was determined using a two-tailed unpaired *t* test followed by the Mann–Whitney test, resulting in a *P*-value significantly less than 0.1. (*D*) Wide-field images of neonatal rat cardiomyocytes (NRCMs) expressing Voltron (Ace2-HaloTag7)-175 M/M175L and labeled with CA-JF_{525} (both at 100 nM concentrations) for a duration of 25 min at 37 °C. (Scale bar, 10 μm.) (*E*) A representative fluorescence trace of NRCMs expressing Voltron-175 M and labeled with CA-JF_{525}. 9 min (54000 frames) recordings at 100 Hz were performed. The gray dashed line represents the time required to photobleach 50% of the original fluorescence of $Voltron_{525}$. (*F*) A representative fluorescence trace of NRCMs expressing Voltron-M175L and labeled with CA-JF_{525}. 15 min (90000 frames) recordings at 100 Hz were performed. The gray dashed line represents the time required to photobleach 50% of the original fluorescence of $Voltron_{525}$-M175L.

Notably, M175D and M175E mutants gave the poorest photon budgets, suggesting that the presence of negative charges nearby the fluorophores tends to lead to faster photobleaching. Aromatic residues like W, F, and Y also appear to have significant negative effects.

Among all the improved mutations, M175L/P/R mutations were selected for further validation in live-cell confocal imaging where the environment is more complex than that of in vitro single-molecule assays. HaloTag was genetically fused to the C-terminus of human histone H2B, and the H2B-HaloTag was transiently expressed in HeLa cells and labeled with CA-TMR or CA-SiR for confocal imaging (Fig. 3*D*). The high expression level of H2B enabled us to systematically compare the photobleaching rates in representative 2 μm × 3 μm patches using samples with comparable initial brightness levels (*SI Appendix*, Fig. S22). Time-lapse confocal imaging indicated that M175L exhibited higher resistance to bleaching than other mutations, especially compared to the wild-type 175 M (Fig. 3*E* and *SI Appendix*, Figs. S23–S26). Notably, the mutant M175L improved the photostability of SiR-HaloTag more than that of TMR-HaloTag. We also tested the robustness of M175L mutation on circularly permuted HaloTag (cpHaloTag), which is a classical strategy to position fluorophores closer to a sensing protein domain for boosted response in sensors (45–47). Under the same H2B-HaloTag bleaching assay, SiR-cpHaloTag M175L showed 4.4-fold higher photostability than the wt SiR-cpHaloTag (*SI Appendix*, Fig. S27). Overall, our results proved that single-site mutation on HaloTag (M175L) brought out a substantial enhancement in the photostability of TMR/SiR-HaloTag.

HaloTag: M175L Improves the Photostability of Advanced Rhodamine Dyes. To meet the evolving demands of cutting-edge biological imaging techniques, a variety of rhodamine derivatives have emerged in the past 20 y. Janelia Fluor (JF) Dyes were devised using azetidine rings as auxochrome of rhodamine dyes which exhibit enhanced brightness and tunable equilibrium between chemical states (20, 48, 49). The replacement of the oxygen atom in the rhodamine core with a carbon atom resulted in the development of CPY with red-shifted spectra (50). Both JF Dyes and CPY exhibit enhanced brightness and photostability while compatible with self-labeling tags, offering a privileged palette for bioimaging. To test the photostability of HaloTag: M175L with advanced rhodamine derivatives, we conducted the H2B bleaching assay with JF_{525}, JF_{669}, JF_{635}, JF_{646}, and CPY. Based on the bleaching curves, HT: M175L-JF exhibited varying degrees of enhanced photostability compared to HT: 175 M-JF (Fig. 4*A* and *SI Appendix*, Fig. S28). Notably, HT: M175L-CPY and HT: M175L-JF_{635} exhibited 4.8-fold improvements in photostability. HT: M175L-JF_{669} and HT: M175L-JF_{646} showed > two-fold enhancement in photostability. HT: M175L-JF_{525} demonstrated the least improvement (1.3-fold) in photostability (Fig. 4*A*, Table 1 and *SI Appendix*, Fig. S28).

The enhanced photostability of the HaloTag-rhodamine system would benefit time-lapse imaging applications, especially functional imaging using chemigenetic sensors (46). For example, voltage imaging serves as a valuable tool for investigating neuronal activities, but its sensors are membranous molecules whose concentrations are relatively low. Therefore, achieving voltage response signals with a high signal-to-noise ratio often necessitates the use of high excitation light intensities, which poses a great challenge for voltage indicators due to photobleaching. Voltron is one of the most widely used hybrid voltage indicators that combines the voltage sensitivity of microbial rhodopsin with the brightness and photostability of JF dyes (Fig. 4*B*). These dyes effectively bind to HaloTag capture protein domains to respond to membrane potential through fluorescence resonance energy transfer (FRET) with rhodopsin (51). $Voltron_{525}$, which uses JF_{525} as an acceptor, exhibited the highest sensitivity among all Voltron-dye combinations. We labeled neonatal rat cardiomyocytes (NRCMs) expressing Voltron-WT (175 M) and Voltron-M175L with JF_{525}-HaloTag ligands respectively and recorded their spontaneous neuronal activities by continuous imaging. The half-life of photobleaching was 560 ± 50 s for $Voltron_{525}$-WT (175 M), compared with 750 ± 50 s for $Voltron_{525}$-M175L (Fig. 4*C*). In two representative sample cells, the cardiomyocyte labeled with $Voltron_{525}$-175 M took 443 seconds for the fluorescence signal to decrease by 50% due to photobleaching (Fig. 4 *D* and *E*). In contrast, the cardiomyocyte labeled with $Voltron_{525}$-M175L was imaged for 840 s before the fluorescence signal decreased by 50% due to photobleaching (Fig. 4 *D* and *F*). These comparative voltage imaging recordings demonstrate that thioether editing translates to an improved performance of HaloTag-based tools.

Finally, we showcase that the photostable HaloTag: M175L synergizes with time-lapse superresolution recording of live-cell dynamics. The mitochondrial outer membrane, inner membrane, and endoplasmic reticulum in U-2 OS cells were labeled with TOMM20-Halo-M175L/WT (175 M)-SiR, PKMO, and mStayGold(J)-SEC61β, respectively (Fig. 5*A* and Movie S1). Using a low-phototoxicity HiS-SIM setup (52), 770 frames of three-color SR images can be captured. During the first stage (until 90% fluorescence retention) of photobleaching, intensity analysis revealed a 5.5-fold increase in the initial photostability for TOMM20-Halo-M175L-SiR compared to the wtHaloTag counterpart (Fig. 5*B*). Notably, the photobleaching of wtHaloTag-SiR slows down afterward. Further analysis of two representative cells indicated that cells expressing TOMM20-Halo-M175L required

Table 1. Photostability of rhodamine derivatives on HaloTag in live-cell confocal imaging

Fluorophore	Excitation wavelength (nm)	Post-objective Laser Power (μW)	Bleaching time (s)* when bound to HaloTag (M175L)	Bleaching time (s)* when bound to HaloTag WT (175 M)	Enhancement factor
JF_{525}	488	14.7	3.1 ± 0.2	2.4 ± 0.1	1.3 ± 0.1
TMR	561	6.7	1.60 ± 0.07	1.64 ± 0.03	0.98 ± 0.04
CPY	561	2.5	116 ± 18	24.1 ± 1.3	4.8 ± 0.8
JF_{635}	640	0.78	31 ± 15	6.6 ± 1.1	4.8 ± 2.4
JF_{646}	640	3.1	60.5 ± 3.0	28.8 ± 2.5	2.1 ± 0.2
SiR	640	6.9	15.6 ± 0.7	5.0 ± 0.4	3.1 ± 0.3
JF_{669}	640	3.1	82.1 ± 8.8	32.5 ± 1.1	2.5 ± 0.3

*Measured by the time at which the fluorescence was bleached by 10%. Pixel dwell time: 10 μs. NA of the objective: 1.45.

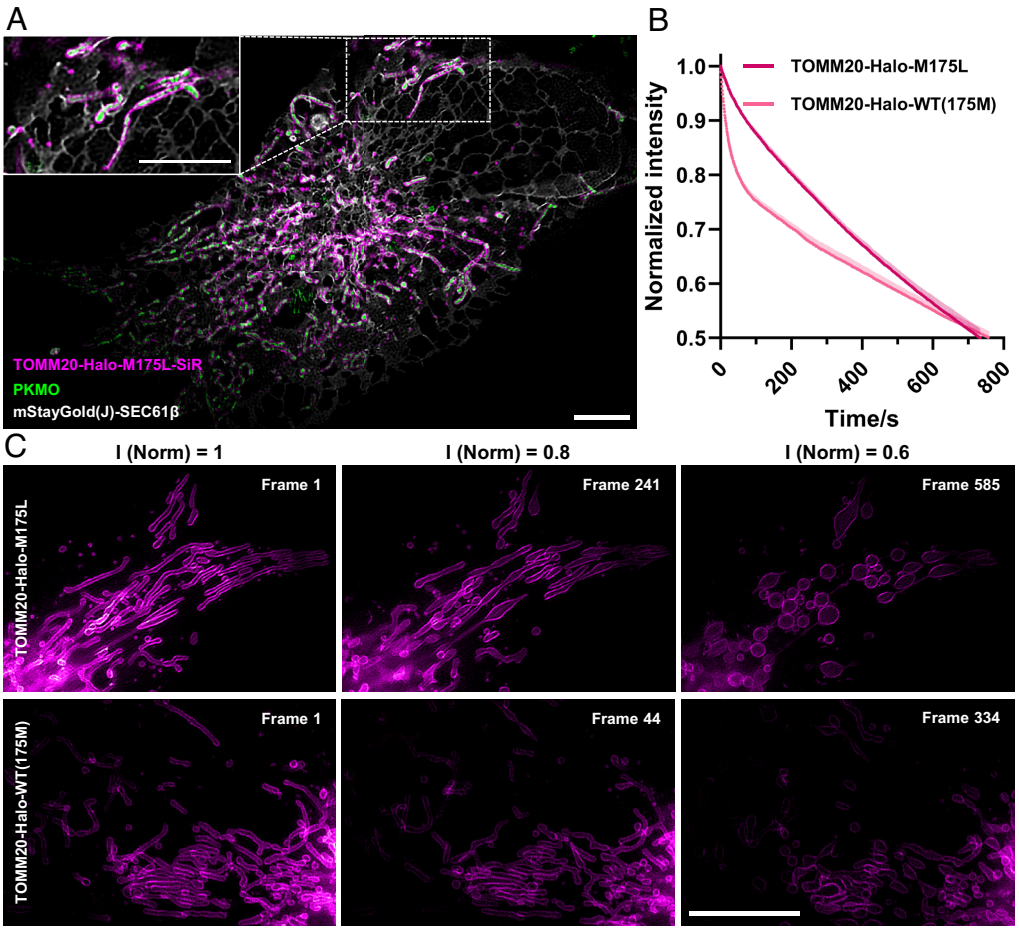

Fig. 5. HaloTag M175L-SiR exhibits enhanced photostability in SIM imaging. (*A*) Three-color SIM imaging of HT: M175L-SiR targeted outer mitochondrial membrane, PKMO labeled inner mitochondrial membrane and mStayGold(J) targeted endoplasmic reticulum. The illumination intensity of the 488 nm, 561 nm, and 638 nm laser was 15.432, 7.716, and 7.716 W·cm^{-2}(985 ms/loop, 10 ms exposure per channel). (Scale bar, 5 μm.) (*B*) Normalized fluorescence intensities of TOMM20-HaloTag-WT (175 M)/M175L using SIM (SEM of five independent experiments is shown as error bars). (*C*) Time-lapse SIM recording of the outer mitochondrial membrane in U-2 OS cells expressing TOMM20-HaloTag-WT (175 M)/M175L labeled with SiR. (Scale bar, 10 μm.)

241 and 585 images to bleach to 80 and 60% of initial intensity, respectively, whereas cell expressing TOMM20-Halo-WT (175 M) reached the same levels after only 44 and 344 images (Fig. 5*C*). Consistently, HT: M175L-SiR was evaluated in both monochromatic and dual-color structured illumination microscopy (SIM), yielding comparable outcomes across various SIM imaging conditions (*SI Appendix*, Figs. S29 and S30). These findings underscore that HaloTag: M175L offers enhanced photostability to SiR when imaged using SIM, making it a general tool for long-term superresolution imaging.

Dye-Sensitized M175 Oxidation Attenuates the Thioether Effect in HaloTag-Based Live-Cell Imaging. In the photobleaching results of the rhodamine-HaloTag conjugates across various cellular imaging conditions, we consistently observed that the difference in photobleaching rates between M175 and M175L was significantly greater in the initial stages compared to later stages and we therefore compared photobleaching rates using only the initial 10% of decay time. Thus, we examined the mechanism of the thioether effect by light-induced protein modifications. HaloTag protein was labeled with SiR-S5, an exchangeable HaloTag Ligand (xHTL) (53), that positions the SiR dye similarly to covalent labeling on the protein surface but allows dye removal after illumination. SDS-PAGE analysis revealed the appearance of high-molecular-weight protein bands after just 5 min illumination with a 620-nm LED lamp in the presence of the dye, indicating cross-linking or putative protein modification (*SI Appendix*, Fig. S31).

Next, we performed electrospray ionization high-resolution mass spectrometry (ESI-HRMS) to detect low-molecular weight modifications and focused on the oxidation with molecular oxygen. The unlabeled full-length protein yielded MS signals with the expected isotopic pattern at M_r 35466.0104 Da (Fig. 6*A*). Illumination for 5, 30, or 180 min in the presence of the dye caused progressive peak broadening and a shift toward higher molecular weights (Fig. 6*A*). Such shift was not observed in absence of the dye even after 180 min illumination (Fig. 6*B*). The illuminated dye-containing samples displayed characteristic oxidation patterns (Δm +15.99, +32.97, +48.97 Da, Fig. 6*C*). Light-induced photooxidation of exposed Met residues is well documented (54) and peptide tandem mass spectrometry (MS/MS) has been used as the method of choice to study such modifications (55). After tryptic digestion, HaloTag peptides were analyzed by ESI-HRMS and mapped against the HaloTag primary sequence, revealing only trace amounts of Met oxidation (Fig. 6 *D* and *E* and *SI Appendix*, Fig. S32). In contrast, labeling with SiR-S5 followed by 620-nm illumination yielded peptides with substantial mono- and dioxidation, notably at M175 (Fig. 6 *D* and *E* and *SI Appendix*, Fig. S33).

Based on these results, we prove a gradual increase in methionine oxidation with longer illumination times and only in the

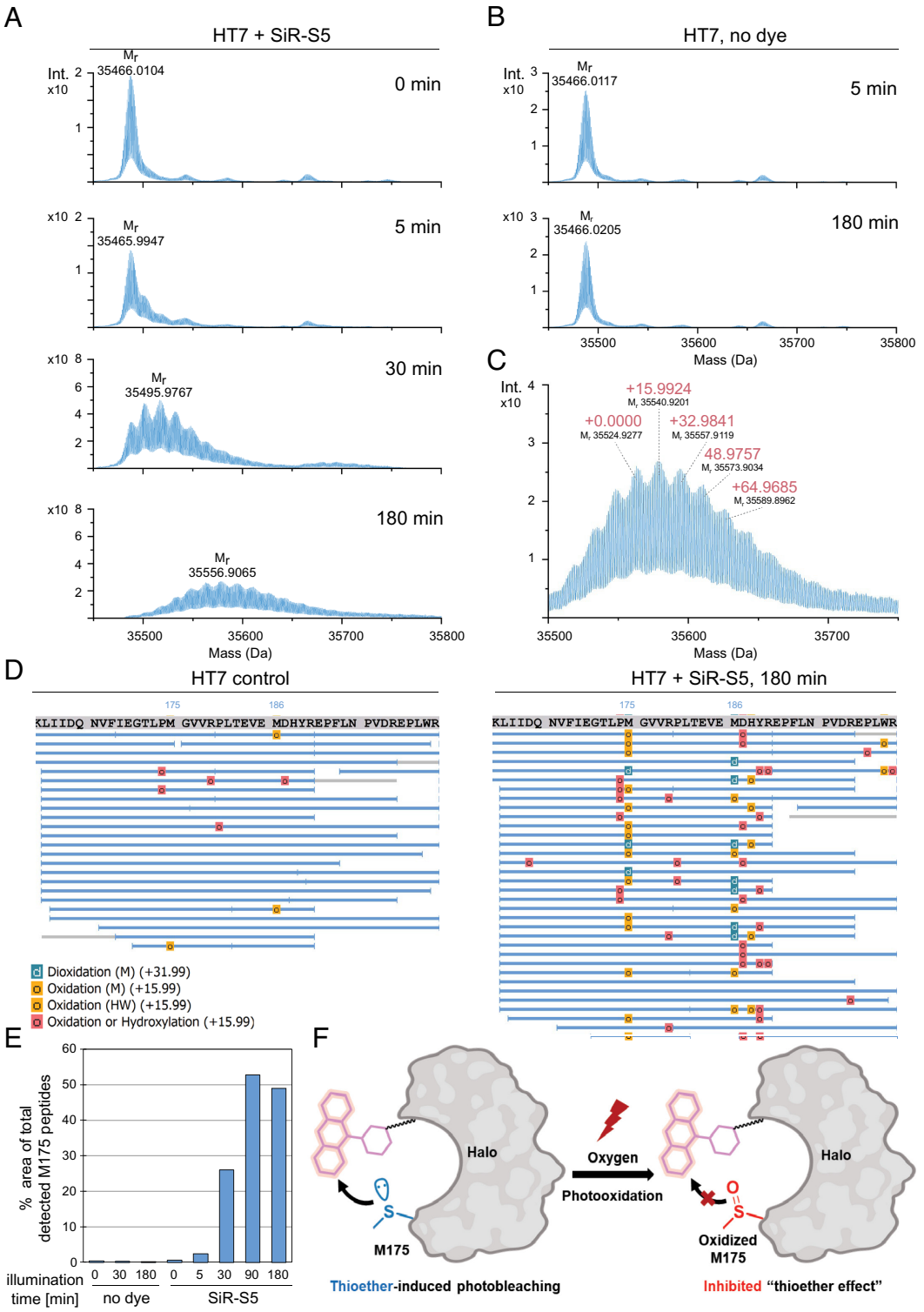

Fig. 6. Mechanistic study on dye-sensitized HaloTag protein photooxidation. Recombinantly expressed His_{10}-TEV-HaloTag7 protein (2.5 μM) was illuminated with a 620 nm LED lamp (4 W) collimated into an optical fiber for different illumination times (0, 5, 30, 90, 180 min) in the presence or absence of a twofold excess of a SiR-conjugated exchangeable HaloTag Ligand (xHTL, SiR-S5, 5 μM). The protein was concentrated and the dye was removed using centrifugal filters. (*A* and *B*) Charge deconvoluted MS spectra of His_{10}-TEV-HaloTag7 (10 μM). Samples were illuminated in the presence (*A*) or absence (*B*) of the dye. The intact protein samples were analyzed by ESI-MS (expected monoisotopic mass = 35465.9103 Da). These experiments have been performed in triplicates with a similar outcome (data not shown). (*C*) Zoomed-in charge deconvoluted MS spectrum of His10-TEV-HaloTag7 after 180 min illumination in dye presence (sample from *A*). A precise protein oxidation pattern (Δm +15.99, +32.97, +48.97 Da) was detected. (*D*) Peptide analysis and oxidation profile. Protein samples were subjected to tryptic digest. Peptides were analyzed by MS and mapped against the HaloTag7 primary sequence. Oxidative protein modifications are shown according to the legend of the untreated (control) and dye-labeled sample after 180 min illumination. Peptides with a -10lgP score ≤ 15 were excluded from the analysis results; gray bars represent partially matched de novo peptides. Qualitative analysis revealed an enrichment of methionine mono- and dioxidation after the irradiation. (*E*) Semiquantitative enrichment of M175 mono-oxidation upon illumination. The percentages of accumulated areas of all mapped peptides bearing M175. (*F*) Photooxidation of M175 disrupts its intrinsic ability to accelerate rhodamine photobleaching.

presence of the dye. We propose a mechanism for the different photobleaching rates in the initial stage, when M175 is presented in the microenvironment of the rhodamine dyes, and at later stages, when M175 is mostly oxidized. As photobleaching progresses, M175 is gradually converted to mono- or dioxidized M175, thereby inhibiting the thioether effect and reducing the difference in photobleaching rates of HaloTag M175 and M175L mutants. (Fig. 6*F*). Corroborating the experimental photobleaching kinetics (Figs. 3 *E* and *F*, 4*A*, 5*B*, and *SI Appendix*, Figs. S27 and S28), this photooxidation process mechanistically supports the hypothesis of thioether photobleaching effect.

Conclusion

In summary, we generalize the "thioether photobleaching effect" to self-labeling protein tags. Editing the thioether group by either electronically tuning the sulfur atom or biochemically eliminating the thioether bond would generally and positively affect the photostability of proximal fluorophores. In time-lapse imaging practice, this thioether-mediated photobleaching enhancement represents an early-phase effect that decays with accumulating methionine residue oxidation. From a photochemistry perspective, this work adds to the emerging topics where the surrounding microenvironment of the fluorophores exerts a profound influence on its optical properties, including fluorescent lifetime, fluorescence quantum yield, and here photobleaching pathways. The photophysical chemistry of thioether with excited fluorophores, however, remains largely elusive and warrants further mechanistic studies. In the context of advancing bioimaging tool development, we showcase thioether editing as a general strategy to mitigate the photobleaching of SLP-labeled fluorophores in time-lapse live-cell imaging. Particularly, by introducing a simple mutation, the HaloTag: M175L renders remarkable enhancements in the photostability of a palette of advanced fluorophores, opening wider space in time-lapse functional imaging and superresolution imaging.

Materials and Methods

Single-Molecule Fluorescence Measurements of Dye Properties. (35, 56) For characterizing the dye properties of proteins during photobleaching, specific labeling was performed using streptavidin and biotinylated proteins. Dye-tag conjugates were prepared by TMR or SiR ligands (10 μM) with proteins of self-labeling tags (5 μM) at 37 °C in PBS buffer for 1 h. For TMP-tag labeling, NADPH (100 μM) and TCEP (1 mM) were added to the labeling buffer. For SNAP-tag labeling, TCEP (1 mM) was added to the labeling buffer.

After labeling, a 20 μL reaction with labeled protein (2 nM) was applied to PEG-passivated slides decorated with biotin-PEG and streptavidin. Excessive unbound complexes were removed by washing with the same buffer as labeling.

Photobleaching procedures were performed on a home-built objective-type TIRF microscope, based on a Nikon Eclipse Ti-E with an EMCCD camera (Andor iXon Ultra 897), and solid-state 532 and 640 nm excitation lasers (Coherent Inc. OBIS Smart Lasers). Fluorescence was collected and spectrally separated using a Dual-Viewer spectral splitter (Photometrics, Inc., Tucson, AZ) with a specific dichroic mirror (T635lpxr, Chroma) and bandpass filters (ET585/65 m for TMR, ET700/75 m for SiR, Chroma). Data were acquired at 100 ms per frame for 400 s at 25 °C without further elaboration. The same batch of labeled samples was measured in at least three parallel experiments to estimate errors for all data. Under the condition of single-molecule imaging, data were recorded in the labeling buffer described above with an oxygen scavenging system, containing 3 mg/mL glucose, 10 units/mL glucose oxidase (Sigma-Aldrich), 1,200 units /mL catalase (Roche), 1 mM cyclooctatetraene (COT, Sigma-Aldrich), 1 mM 4-nitrobenzylalcohol (NBA, Sigma-Aldrich), 1.5 mM 6-hydroxy-2,5,7,8-tetramethyl-chromane-2-carboxyl ic acid (Trolox, Sigma-Aldrich, added from a concentrated DMSO stock solution) under 50 W/cm^2 for 532-nm excitation TMR (or 40 W/cm^2 for 640-nm excitation SiR) labeled samples. The laser was reduced to 5 or 4 W/cm^2 for simulating the cell imaging.

Confocal Imaging for Measuring Bulk Photobleaching. Prior to imaging, HeLa cells expressing H2B-HaloTag/SNAP-Tag were stained with Halo dyes and BG dyes at a final concentration of 100 to 250 nM and then were rinsed with PBS three times before imaging. All confocal imaging experiments were performed with STEDYCON STED microscopes (Abberior Instruments GmbH, Göttingen, Germany) equipped with a CFI Plan Apochromat Lambda D 100x oil, NA1.45 objective (Nikon, Tokyo, Japan). The fluorescence signal was accumulated over 2 to 5 line steps. Imaging parameters were adjusted based on the individual samples. Pixel sizes of 100 nm were used in the confocal mode, each line was scanned five times (line accumulations) and dwell times were acquired for five times. The pinhole was set to 1.0 AU. For photobleaching analysis, 5 to 6 patches of 2 μm × 3 μm from 2 to 3 different cells were acquired for each repeat. 9,000 frames were acquired for each patch with a dwell time of 10 μs per pixel and a line accumulation of 1 or 10.

Voltage Imaging. Neonatal rat cardiomyocytes expressing Voltron (Ace2-HaloTag7) and Voltron-M175L were labeled with JF_{525} (100 nM in DMEM) at 37 °C with 5% CO_2 for 25 min. After removing the staining solution, the cells were then washed with HBSS once and maintained in a fresh culture medium. Voltron imaging was performed with an inverted fluorescence microscope (Nikon-TiE) equipped with an objective CFI Plan Fluor 40× oil, NA 1.3 (Nikon, Tokyo, Japan), one laser line (561 nm, Coherent OBIS), and one scientific CMOS camera (Hamamatsu ORCA-Flash 4.0 v2). The microscope, laser, and camera were controlled by LabVIEW software (National Instruments, 15.0 version). Images were captured using a camera on 2 × 2 pixel binning and a 100-ms exposure duration. Images were analyzed using ImageJ/Fiji (version 1.52d).

HiS-SIM Imaging. U-2 OS cells were cultured in confocal dishes, and plasmids were transfected after 24 h when the cell confluence reached 60% with Lipo3000. After 48 h, cells were maintained at 37 °C and 5% CO_2 in a humidified chamber for live SIM imaging. Superresolution imaging of cells was performed using commercialized HiS-SIM, termed HiS-SIM (High Intelligent and Sensitive SIM) provided by Guangzhou CSR Biotech Co. Ltd. Images were acquired using a 100×/1.5 NA oil immersion objective (Olympus). For three-color imaging, 488, 561, and 638 nm lasers were jointly used. The images were acquired sequentially at alternate 488, 561, and 638 nm excitation and 10 ms exposure using the Andor Solis software. SIM images were collected and analyzed as described previously. Wiener and Sparse deconvolution were carried out to further improve the image quality (52, 57).

More detailed methods including chemical synthesis of TMP-3.1 and Rhodamine-Motif, plasmids construction, protein production and purification, preparation of PEG-passivated slides, cell culture and transfection, in vitro protein labeling of eDHFR, HaloTag photooxidation assay, intact ESI-HRMS protein analysis, protein digestion, LC–MSMS analysis and peptide mapping, LC–MS analysis, data analysis, and ethics approval and consent to participate are described in *SI Appendix*.

Data, Materials, and Software Availability. All study data are included in the article and/or supporting information.

ACKNOWLEDGMENTS. This project was supported by funds from National Key R&D Program of China (2024YFA1306200 to C.C., 2021YFF0502904 to Z.C., and 2020YFA0509502 to W.D.), the Beijing Municipal Science & Technology Commission (Project: Z221100003422013 to Z.C.), the National Natural Science Foundation of China (Grants Nos. 22425701, 22277063, and 22061160466 to C.C., 32170566 to W.D., and 22007054 and 32370391 to W.W.), the Beijing Frontier Research Center for Biological Structure (to C.C.), the Max Planck Society and the Deutsche Forschungsgemeinschaft (DFG, German Research Foundation), and Beijing National Laboratory for Molecular Sciences (BNLMS202407 to Z.C.). We thank Prof. Heping Cheng for the guidance on cardiomyocyte isolation, Dr. Qinsi Zheng for valuable discussions, and Prof. Kai Johnsson for experimental support and critical advice. We thank the Metabolic Mass Spectrometry Platform of Institute of Molecular Medicine, the analytical instrumentation center of Peking University, and the NMR facility of National Center for Protein Sciences at Peking University. We also thank Guangzhou Computational Super-resolution Biotech Co. Ltd for offering a superresolution microscope (HiS-SIM) and assistance in data acquisition and image reconstruction. We thank Juliana Kling for assisting the mass spectrometry workflow and Andrea Bergner for providing materials (both MPIMF).

Author affiliations: [a]Peking-Tsinghua Center for Life Science, Academy for Advanced Interdisciplinary Studies, Peking University, Beijing 100871, China; [b]Institute of Molecular Medicine, National Biomedical Imaging Center, Beijing Key Laboratory of Cardiometabolic Molecular Medicine, College of Future Technology, Peking University, Beijing 100871, China; [c]State Key Laboratory of Membrane Biology, Beijing Frontier Research Center for Biological Structure, School of Life Sciences, Tsinghua University, Beijing 100084, China; [d]Department of Chemical Biology, Max Planck Institute for Medical Research, Heidelberg 69120, Germany; [e]Biomedical Pioneering Innovation Center, Peking University, Beijing 100871, China; [f]Academy for Advanced Interdisciplinary Studies, Peking University, Beijing 100871, China; [g]Mass Spectrometry Core Facility, Max Planck Institute for Medical Research, Heidelberg 69120, Germany; [h]Peking University-Nanjing Institute of Translational Medicine, Nanjing 211800, China; [i]Genvivo Biotech, Nanjing 211800, China; [j]School of Life Sciences, Technology Center for Protein Sciences, Tsinghua University, Beijing 100084, China; [k]State Key Laboratory of Membrane Biology, Peking University School of Life Sciences, Beijing 100871, China; [l]IDG/McGovern Institute for Brain Research at Peking University, Beijing 100871, China; [m]Chinese Institute for Brain Research, Beijing 102206, China; [n]College of Chemistry and Molecular Engineering, Synthetic and Functional Biomolecules Center, Beijing National Laboratory for Molecular Sciences, Key Laboratory of Bioorganic Chemistry and Molecular Engineering of the Ministry of Education, Peking University, Beijing 100871, China; and [o]Beijing National Laboratory for Molecular Sciences, Beijing 100190, China

Author contributions: Z.C., C.C., and Y.Z. conceived the project; Y.Z., J.Z., J.D., and J.S. performed the chemical synthesis under the supervision of Z.C.; J.L., Y.Z., and K.Z. carried out the confocal imaging under the supervision of Z.C.; Y.H., C.Y., and B.W. performed single-molecule fluorescence experiments under the supervision of C.C., W.D., and W.W.; J.L. conducted plasmid construction, protein expression, and extraction, as well as SIM imaging; J.L. performed voltage imaging experiments under the supervision of P.Z.; Y.L. provided key fluorescent dyes; Y.L. supervised the related imaging experiments; J.K., S.F., and T.R. carried out dye-sensitized protein photooxidation and ESI-MS experiments; J.L., Y.Z., Y.H., J.K., and C.Y. analyzed the data; and Y.Z., J.L., Y.H., J.K., C.C., and Z.C. wrote the manuscript.

1. C. Jing, V. W. Cornish, Chemical tags for labeling proteins inside living cells. *Acc. Chem. Res.* **44**, 784–792 (2011).
2. Y. Takaoka, A. Ojida, I. Hamachi, Protein organic chemistry and applications for labeling and engineering in live-cell systems. *Angew. Chem. Int. Ed.* **52**, 4088–4106 (2013).
3. C. A. Hoelzel, X. Zhang, Visualizing and manipulating biological processes by using HaloTag and SNAP-Tag technologies. *ChemBioChem* **21**, 1935–1946 (2020).
4. D. Saimi, Z. Chen, Chemical tags and beyond: Live-cell protein labeling technologies for modern optical imaging. *Smart Mol.* **1**, e20230002 (2023).
5. G. V. Los *et al.*, HaloTag: A novel protein labeling technology for cell imaging and protein analysis. *ACS Chem. Biol.* **3**, 373–382 (2008).
6. A. Keppler *et al.*, A general method for the covalent labeling of fusion proteins with small molecules in vivo. *Nat. Biotechnol.* **21**, 86–89 (2003).
7. L. W. Miller, Y. Cai, M. P. Sheetz, V. W. Cornish, In vivo protein labeling with trimethoprim conjugates: A flexible chemical tag. *Nat. Methods* **2**, 255–257 (2005).
8. J. Mo *et al.*, Third-generation covalent TMP-Tag for fast labeling and multiplexed imaging of cellular proteins. *Angew. Chem. Int. Ed.* **61**, e202207905 (2022).
9. A. Cook, F. Walterspiel, C. Deo, HaloTag-based reporters for fluorescence imaging and biosensing. *Nat. Chem. Biol.* **24**, e202300022 (2023).
10. Q. Zheng *et al.*, Ultra-stable organic fluorophores for single-molecule research. *Chem. Soc. Rev.* **43**, 1044–1056 (2014).
11. M. Lsselstein *et al.*, Self-healing dyes–Keeping the promise? *J. Phys. Chem. Lett.* **11**, 4462-4480 (2020).
12. Y. Zhang, J. Ling, T. Liu, Z. Chen, Lumos maxima–How robust fluorophores resist photobleaching? *Curr. Opin. Chem. Biol.* **79**, 102439 (2024).
13. R. R. Nani, J. A. Kelley, J. Ivanic, M. J. Schnermann, Reactive species involved in the regioselective photooxidation of heptamethine cyanines. *Chem. Sci.* **6**, 6556–6563 (2015).
14. A. N. Butkevich, M. L. Bossi, G. V. Lukinaviccius, S. Hell, Triarylmethane fluorophores resistant to oxidative photobluing. *J. Am. Chem. Soc.* **141**, 981-989 (2018).
15. R. Dave, D. S. Terry, J. B. Munro, S. C. Blanchard, Mitigating unwanted photophysical processes for improved single-molecule fluorescence imaging. *Biophys. J.* **96**, 2371–2381 (2009).
16. T. Cordes, A. Maiser, C. Steinhauer, L. Schermelleh, P. Tinnefeld, Mechanisms and advancement of antifading agents for fluorescence microscopy and single-molecule spectroscopy. *Phys. Chem. Chem. Phys.* **13**, 6699–6709 (2011).
17. Z. Yang *et al.*, Cyclooctatetraene-conjugated cyanine mitochondrial probes minimize phototoxicity in fluorescence and nanoscopic imaging. *Chem. Sci.* **11**, 8506–8516 (2020).
18. T. Liu *et al.*, Gentle rhodamines for live-cell fluorescence microscopy. *ACS Cent. Sci.* **10**, 1933–1944 (2024).
19. X. Song, A. Johnson, J. Foley, 7-Azabicyclo [2.2.1] heptane as a unique and effective dialkylamino auxochrome moiety: Demonstration in a fluorescent rhodamine dye. *J. Am. Chem. Soc.* **130**, 17652-17653 (2008).
20. J. B. Grimm *et al.*, A general method to improve fluorophores for live-cell and single-molecule microscopy. *Nat. Methods* **12**, 244–250 (2015).
21. M. Grzybowski *et al.*, A highly photostable near-infrared labeling agent based on a phospha-rhodamine for long-term and deep imaging. *Angew. Chem. Int. Ed.* **57**, 10137-10141 (2018).
22. Z. Ye *et al.*, Quaternary piperazine-substituted rhodamines with enhanced brightness for super-resolution imaging. *J. Am. Chem. Soc.* **141**, 14491–14495 (2019).
23. X. Lv, C. Gao, T. Han, H. Shi, W. Guo, Improving the quantum yields of fluorophores by inhibiting twisted intramolecular charge transfer using electron-withdrawing group-functionalized piperidine auxochromes. *Chem. Commun.* **56**, 715–718 (2020).
24. D. H. Li, C. L. Schreiber, B. D. Smith, Sterically shielded heptamethine cyanine dyes for bioconjugation and high performance near-infrared fluorescence imaging. *Angew. Chem. Int. Ed.* **59**, 12154–12161 (2020).
25. J. B. Grimm *et al.*, A general method to improve fluorophores using deuterated auxochromes. *JACS Au* **1**, 690–696 (2021).
26. K. Roßmann *et al.*, N-Methyl deuterated rhodamines for protein labelling in sensitive fluorescence microscopy. *Chem. Sci.* **13**, 8605–8617 (2022).
27. G. Jiang *et al.*, A synergistic strategy to develop photostable and bright dyes with long Stokes shift for nanoscopy. *Nat. Commun.* **13**, 2264 (2022).
28. H. Chen, S. S. Ahsan, M. E. B. Santiago-Berrios, H. D. Abruña, W. W. Webb, Mechanisms of quenching of alexa fluorophores by natural amino acids. *J. Am. Chem. Soc.* **132**, 7244–7245 (2010).
29. M. S. Frei *et al.*, Engineered HaloTag variants for fluorescence lifetime multiplexing. *Nat. Methods* **19**, 65–70 (2022).
30. G. Lukinavičius *et al.*, A near-infrared fluorophore for live-cell super-resolution microscopy of cellular proteins. *Nat. Chem.* **5**, 132–139 (2013).
31. L. Wang *et al.*, A general strategy to develop cell permeable and fluorogenic probes for multicolour nanoscopy. *Nat. Chem.* **12**, 165–172 (2020).
32. M. Hirano *et al.*, A highly photostable and bright green fluorescent protein. *Nat. Biotechnol.* **40**, 1132–1142 (2022).
33. S. Niekamp, N. Stuurman, R. D. Vale, A 6-nm ultra-photostable DNA FluoroCube for fluorescence imaging. *Nat. Methods* **17**, 437–441 (2020).
34. A. T. Blanchard *et al.*, Ultra-photostable DNA FluoroCubes: Mechanism of photostability and compatibility with FRET and dark quenching. *Nano Lett.* **22**, 6235–6244 (2022).
35. Y. Zhang *et al.*, General strategy to improve the photon budget of thiol-conjugated cyanine dyes. *J. Am. Chem. Soc.* **145**, 4187–4198 (2023).
36. D. M. Presman *et al.*, Quantifying transcription factor binding dynamics at the single-molecule level in live cells. *Methods* **123**, 76–88 (2017).
37. R. S. Erdmann *et al.*, Labeling strategies matter for super-resolution microscopy: A comparison between HaloTags and SNAP-tags. *Cell Chem. Biol.* **26**, 584–592.e586 (2019).
38. S. S. Gallagher, J. E. Sable, M. P. Sheetz, V. W. Cornish, An in vivo covalent TMP–Tag based on proximity-induced reactivity. *ACS Chem. Biol.* **4**, 547–556 (2009).
39. Z. Chen, C. Jing, S. S. Gallagher, M. P. Sheetz, V. W. Cornish, Second-generation covalent TMP-Tag for live cell imaging. *J. Am. Chem. Soc.* **134**, 13692–13699 (2012).
40. J. Dong, L. Krasnova, M.G. Finn, K. B. Sharpless, Sulfur(VI) Fluoride Exchange (SuFEx): Another good reaction for click chemistry. *Angew. Chem. Int. Ed.* **53**, 9430–9448 (2014).
41. T. Tamura *et al.*, Rapid labelling and covalent inhibition of intracellular native proteins using ligand-directed N-acyl-N-alkyl sulfonamide. *Nat. Commun.* **9**, 1870 (2018).
42. S. Li, N. Wang, B. Yu, W. Sun, L. Wang, Genetically encoded chemical crosslinking of carbohydrate. *Nat. Chem.* **15**, 33–42 (2023).
43. B. Yang *et al.*, Proximity-enhanced SuFEx chemical cross-linker for specific and multitargeting cross-linking mass spectrometry. *Proc. Natl. Acad. Sci. U.S.A.* 115, 11162–11167 (2018).
44. J. Wilhelm *et al.*, Kinetic and structural characterization of the self-labeling protein tags HaloTag7, SNAP-tag, and CLIP-tag. *Biochemistry* **60**, 2560–2575 (2021).
45. G. S. Baird, D. A. Zacharias, R. Y. Tsien, Circular permutation and receptor insertion within green fluorescent proteins. *Proc. Natl. Acad. Sci. U.S.A.* 96, 11241–11246 (1999).
46. C. Deo *et al.*, The HaloTag as a general scaffold for far-red tunable chemigenetic indicators. *Nat. Chem. Biol.* **17**, 718–723 (2021).
47. M.-C. Huppertz *et al.*, Recording physiological history of cells with chemical labeling. *Science* **383**, 890–897 (2024).
48. J. B. Grimm *et al.*, A general method to fine-tune fluorophores for live-cell and in vivo imaging. *Nat. Methods* **14**, 987–994 (2017).
49. J. B. Grimm, T. A. Brown, A. N. Tkachuk, L. D. Lavis, General synthetic method for Si-fluoresceins and Si-rhodamines. *ACS Cent. Sci.* **3**, 975–985 (2017).
50. A. N. Butkevich *et al.*, Fluorescent rhodamines and fluorogenic carbopyronines for super-resolution STED microscopy in living cells. *Angew. Chem. Int. Ed.* **55**, 3290–3294 (2016).
51. A. S. Abdelfattah *et al.*, Bright and photostable chemigenetic indicators for extended in vivo voltage imaging. *Science* **365**, 699–704 (2019).
52. X. Huang *et al.*, Fast, long-term, super-resolution imaging with Hessian structured illumination microscopy. *Nat. Biotechnol.* **36**, 451–459 (2018).
53. J. Kompa *et al.*, Exchangeable HaloTag Ligands for super-resolution fluorescence microscopy. *J. Am. Chem. Soc.* **145**, 3075–3083 (2023).
54. G. Jori, G. Galiazzo, A. M. Tamburro, E. Scoffone, Dye-sensitized photooxidation as a tool for determining the degree of exposure of amino acid residues in proteins. *J. Biol. Chem.* **245**, 3375–3383 (1970).
55. Z. Zhang *et al.*, A mass spectrometric characterization of light-induced modifications in therapeutic proteins. *J. Pharm. Sci.* **111**, 1556–1564 (2022).
56. S. Peng, R. Sun, W. Wang, C. Chen, Single-molecule photoactivation FRET: A general and easy-to-implement approach to break the concentration barrier. *Angew. Chem. Int. Ed.* **56**, 6882–6885 (2017).
57. W. Zhao *et al.*, Sparse deconvolution improves the resolution of live-cell super-resolution fluorescence microscopy. *Nat. Biotechnol.* **40**, 606–617 (2022).